Direct multi-resolution estimation of ego-motion and structure from motion

K. J. Hanna

David Sarnoff Research Center

Subsidiary of SRI International

Princeton, NJ 08543-5300, U.S.A.

Abstract

This paper describes an iterative algorithm that estimates the motion of a camera through an environment directly from brightness derivatives of an image pair. A global ego-motion constraint is combined with the local brightness constancy constraint to relate local surface models with the global ego-motion model and local brightness derivatives. In an iterative process, we first refine the local surface models using the ego-motion as a constraint, and then refine the ego-motion model using the local surface models as constraints. We perform this analysis at multiple resolutions. We show how information from local corner-like and edge-like image structures contribute to the refinement of the global ego-motion estimate, and how the ego-motion constraint can help resolve local motion ambiguities that arise from the aperture problem. Results of the algorithm are shown on uncalibrated outdoor image sequences, and also on a computer-rendered image sequence.

1 Introduction

The ego-motion of a camera moving through the environment provides useful information for tasks like moving-obstacle detection and navigation. For moving-obstacle detection, local inconsistencies in the ego-motion model can pinpoint some potential obstacles [Thompson and Pong, 1990]. For navigation, the ego-motion might be used to estimate the surface orientation of an approaching object like a road or a wall.

One approach to recovering ego-motion is to fit a global ego-motion model to a flow field computed from an image pair. Heeger and Jepson proposed an ego-motion recovery scheme that used both image flow information and local image gradient information [Heeger and Jepson, 1990]. The contribution of each flow vector to the ego-motion model was weighted by the local image gradient to reduce errors in the recovered ego-motion estimate that can arise from local ambiguities in image flow from the aperture problem.

In the method presented in this paper, image flow is bypassed as the intermediary between local image brightness changes and the global ego-motion constraint. The brightness constancy constraint is combined with the ego-motion constraint to relate local-planar or local-constant-depth surface models with an ego-motion model and local brightness derivatives. Beginning with initial estimates of the ego-motion and the local surface parameters, the local surface models are refined using the global ego-motion model as a constraint. The global ego-motion model is then refined using the local surface models as constraints. Section 2 describes the algorithm in detail. Adiv described a similar method, but a local-constant-depth model was fitted to a pre-computed flow field rather than directly to image brightness derivatives [Adiv, 1985]. Negahdaripour and Horn have already proposed a direct ego-motion and surface-estimation technique, but only the case of a single surface and ego-motion model within a region are considered [Negahdaripour and Horn, 1987]. Heel's work on direct estimation of ego-motion and local structure is similar [Heel, 1990], but we make the contributions of multi-resolution analysis, and we also show how information from different types of local image structure interact with the ego-motion constraint.

Section 3 shows how local information from edge-like and corner-like image structures contribute to the refinement of the ego-motion estimate, and how the ego-motion estimate contributes to the refinement of the local surface models. We conclude that local ambiguities in image motion arising from the aperture problem do not contribute to errors in the ego-motion estimate, and that the ego-motion constraint can help resolve such local motion ambiguities.

Section 4 presents results of the algorithm on computer-rendered and real image sequences. In these results, local surface models are fitted to 5×5 pixel overlapping windows and the ego-motion model is fitted across the entire image. As part of a vehicle navigation system, analysis would be restricted to a number of larger local windows directed purposively at image regions like the road ahead or an oncoming object [Burt et al. ,1990].

2 Algorithm Description

2.1 Relating image brightness to local surface models and an ego-motion model

From the first order Taylor's expansion of the brightness constancy assumption, the brightness constraint equation is

$$\nabla I^\mathsf{T} du + I_t = 0, \tag{1}$$

where ∇I is the gradient vector of the image brightness values, du is the incremental image motion vector, and I_t is the temporal derivative of the image brightness values (see [Horn, 1986] for example). Using the perspective projection camera model and the derivative of the 3-D position of a moving object (see [Horn, 1986] for example), the image motion, u, of a static object that results from camera translation T and camera rotation Ω can be written as

$$u = KT\tilde{Z} + A\Omega, \tag{2}$$

where $\tilde{Z} = 1/Z$, Z is the depth of the object,

$$
\begin{aligned}
K &= \begin{pmatrix} -f & 0 & x \\ 0 & -f & y \end{pmatrix}, \\
A &= \begin{pmatrix} \frac{xy}{f} & -(f + \frac{x^2}{f}) & y \\ (f + \frac{y^2}{f}) & -\frac{xy}{f} & -x \end{pmatrix}, \quad (3)
\end{aligned}
$$

and x, y are image coordinates and f is the focal length of the camera.

For a local planar patch model,

$$R^\mathsf{T} P = 1, \quad R = (X, Y, Z)^\mathsf{T}, \quad P = (a, b, c)^\mathsf{T}, \tag{4}$$

where R^T is a point in world coordinates and P defines the orientation and depth of the plane. By combining equation 4 with the standard perspective projection equations, $x = Xf/Z$, $y = Yf/Z$, and by eliminating X, Y, we get

$$\tilde{Z} = F^\mathsf{T} P, \quad F = \left(\frac{x}{f}, \frac{y}{f}, 1\right)^\mathsf{T}. \tag{5}$$

Inserting equation 5 into equation 2 gives image motion in terms of camera ego-motion, local surface orientation and depth:

$$u = KTF^\mathsf{T} P + A\Omega. \tag{6}$$

From a previous resolution or iteration we might have an estimate of the global ego-motion parameters, T_0, Ω_0, and also an estimate, P_0, for each local surface model. Equation 6 can be used to write an incremental ego-motion equation:

$$
\begin{aligned}
du &= \left(KTF^\mathsf{T} P + A\Omega\right) - u_0 \\
&= \left(KTF^\mathsf{T} P + A\Omega\right) - \left(KT_0F^\mathsf{T} P_0 + A\Omega_0\right), \quad (7)
\end{aligned}
$$

where u_0 is the image motion corresponding to the previous estimates of the local surface and ego-motion models. Inserting this incremental ego-motion equation into the brightness constraint equation (equation 1), we get

$$
\begin{aligned}
\nabla I^\mathsf{T} KTF^\mathsf{T} P + \nabla I^\mathsf{T} A\Omega - \\
\nabla I^\mathsf{T} KT_0F^\mathsf{T} P_0 - \nabla I^\mathsf{T} A\Omega_0 + I_t &= 0. \quad (8)
\end{aligned}
$$

The error in this equation is used to refine both the local surface models and the global ego-motion model. Specifically, the least-squared error in equation 8 is minimised with respect to the local surface parameters over each local region. The least squares error is then minimised with respect to the ego-motion parameters over all the local regions.

2.2 Local Minimisation

In each local image region, we minimise the least squares error measure

$$
\begin{aligned}
e_{local} = \sum_{local} \big[\nabla I^\mathsf{T} KTF^\mathsf{T} P + \nabla I^\mathsf{T} A\Omega - \\
\nabla I^\mathsf{T} KT_0F^\mathsf{T} P_0 - \nabla I^\mathsf{T} A\Omega_0 + I_t \big]^2 \quad (9)
\end{aligned}
$$

with respect to P. Differentiating equation 9 with respect to P gives

$$
\begin{aligned}
\frac{de}{dP} = 2\sum_{local} \nabla I^\mathsf{T} KTF \big[\nabla I^\mathsf{T} KTF^\mathsf{T} P + \nabla I^\mathsf{T} A\Omega - \\
\nabla I^\mathsf{T} KT_0F^\mathsf{T} P_0 - \nabla I^\mathsf{T} A\Omega_0 + I_t \big]. \quad (10)
\end{aligned}
$$

Setting this to zero and solving for P gives

$$
\begin{aligned}
P_{min} = -G^{-1}\sum_{local} \nabla I^\mathsf{T} KTF \big[\nabla I^\mathsf{T} A\Omega - \\
\nabla I^\mathsf{T} KTF^\mathsf{T} P_0 - \nabla I^\mathsf{T} A\Omega_0 + I_t \big], \quad (11)
\end{aligned}
$$

where

$$G = \sum_{local} \left(\nabla I^\mathsf{T} KT\right)^2 FF^\mathsf{T}, \tag{12}$$

and where G^{-1} is the inverse of G. For the results presented in this paper, the planar patch model is simplified to a constant depth model so that $P = (0, 0, c)^\mathsf{T}$. Equation 11 then becomes

$$c_{min} =$$

$$\frac{-\sum_{local} \nabla I^\mathsf{T} KT \left[\nabla I^\mathsf{T} A\Omega - \nabla I^\mathsf{T} KT_0 c_0 - \nabla I^\mathsf{T} A\Omega_0 + I_t\right]}{\sum_{local}(\nabla I^\mathsf{T} KT)^2},$$

$$\tag{13}$$

where c_0 is an estimate of the local depth from a previous scale or iteration.

157

2.3 Global minimisation

In the global image region, we minimise the least squares error measure

$$e_{global} = \sum_{global} \left[\nabla I^\top K T c_{min} + \nabla I^\top A\Omega - \right.$$

$$\left. \nabla I^\top K T_0 c_0 - \nabla I^\top A\Omega_0 + I_t \right]^2 \quad (14)$$

with respect to T and Ω, where c_{min} for each local region is given by equation 13. Equation 14 is valid only for the simplified local-constant-depth model. As formulated here, the error is quadratic in Ω but non-quadratic in T, and a non-linear minimisation technique is required. In the current implementation of the algorithm, we perform Gauss-Newton minimisation using Ω_0 and T_0 as initial starting values. If initial estimates Ω_0, T_0 are not available (from a previous frame in a sequence for example), we insert trial translation values into equation 14, solve for $\Omega - \Omega_0$ (in closed form since equation 14 is quadratic in $\Omega - \Omega_0$) and choose as our initial estimates the T and $\Omega - \Omega_0$ that give the lowest error in equation 14.

2.4 Algorithm Summary

We perform the local and global minimisation within a multi-resolution pyramid framework. In summary, the algorithm performs the following steps:

1. Initialise local surface parameters and ego-motion parameters.

2. Beginning with a coarse resolution of a Gaussian or Laplacian pyramid, warp the first image towards the second image using equation 6 with the current estimates of the local surface parameters and global ego-motion parameters.

3. Refine all local surface parameters using equation 13, and use equation 14 to refine the ego-motion parameters by performing one Gauss-Newton minimisation step.

4. Repeat steps 2 and 3 several times (we currently use 10 iterations).

5. Expand the local surface parameters into the next finest resolution of the pyramid.

6. Repeat steps 2,3,4,5 at the next finest resolution of the pyramid using the current estimates of the ego-motion parameters as the initial starting values.

3 Discussion

In the local minimisation, the global ego-motion constraint is constraining the refinement of the surface parameters locally. Conversely in the global minimisation, the local constraints provided by local image structures constrain the refinement of the global ego-motion parameters. This section investigates the interaction between local and global constraints at local edge-like and corner-like image structures.

3.1 Global constraints on local motion estimates

In the first part of the algorithm, the ego-motion constraint and the local image brightness derivatives are used to refine each local surface parameter, c. The incremental ego-motion equation (equation 7) can be rewritten for the simplified local-constant-depth model so that

$$du = (KTc + A\Omega) - (KT_0 c_0 + A\Omega_0). \quad (15)$$

We evaluate this expression at $\Omega = \Omega_0$ and $T = T_0$ so that

$$du_0 = KT_0 (c - c_0), \quad (16)$$

where du_0 is the incremental motion introduced by an increment in the parameter c. Therefore, the increment in local motion is constrained to lie along a line in velocity space in the direction of vector KT_0 (the ego-motion constraint line). The vector KT_0 points towards the current estimate of the focus-of-expansion of the image pair.

Within a local region containing a single edge-like image structure, the brightness constraint equation constrains the motion to lie along a line in velocity space in the direction of the edge (perpendicular to ∇I) (see [Horn, 1986] for example). By combining the ego-motion and brightness motion constraint, the surface parameter, c, is refined such that the incremental motion introduced by the refinement lies at the intersection of the ego-motion constraint line and the local brightness constraint line. In this case, a local motion ambiguity arising from the aperture problem has been resolved using only the ego-motion constraint. However, local motion ambiguities cannot be resolved using the ego-motion constraint when the ego-motion constraint line and the local motion constraint line are parallel. In this case, $\sum_{local} \left(\nabla I^\top K T_0 \right)^2 \approx 0$, and the denominator in equation 13 tends to zero. The physical interpretation is that the local edge structure is aligned in the direction of the current estimate of the focus-of-expansion. The local surface parameter

158

cannot be refined reliably because the ego-motion estimate adds little or no constraint to the local brightness constraint. In the current implementation of the algorithm, the local surface parameter is not refined if the denominator in equation 13 is below a threshold.

Within a local region containing a corner-like image structure, both motion components can be resolved from local information [Nagel, 1987], and the local brightness constraint constrains the incremental motion to lie at a single point in velocity space. However, the ego-motion estimate constrains the incremental motion to lie along the ego-motion constraint line in velocity space. If the point and line intersect in velocity space, then the incremental motion introduced by the refinement corresponds to the point in velocity space. If the point and line do not intersect, then the incremental motion lies between the line and the point in velocity space.

3.2 Local constraints on the global ego-motion estimate

Different types of local image structure contribute differently to the refinement of the global ego-motion estimate.

Within a local region containing a single edge-like image structure, the brightness constraint equation (equation 1) shows that the error in the equation will remain constant for any du that is perpendicular to the gradient vector (∇I) of the edge. As a result, only the local motion component normal to the edge is used to refine the global ego-motion estimate. Since there is no contribution from the motion component along the edge direction, we expect less errors in the global ego-motion estimate caused by local motion ambiguities arising from the aperture problem. Heeger and Jepson achieved a similar effect by disregarding flow field components perpendicular to the local image gradient [Heeger and Jepson, 1990].

Within a local region containing a corner-like image structure, both motion components can be resolved from only local information, and both motion components contribute to the refinement of the global ego-motion estimate.

3.3 Multi-resolution Analysis

We use a Gaussian or Laplacian pyramid [Burt, 1983] to refine the ego-motion estimate and local surface parameters at multiple resolutions. In the pyramid framework, large pixel displacements at the resolution of the original image are represented as

small pixel displacements at coarse resolutions. Therefore, the first order Taylor's expansion of the brightness constancy constraint (equation 1 - approximately true only for small du) becomes valid at coarse resolutions even when the image motion is large at the original resolution [Kearney et al., 1987]. The local depth estimates from previous resolutions are used to bring the image pair into closer registration at the next finest resolution. As a result, we expect the first order Taylor's expansion to be valid at all resolutions of analysis in the pyramid, disregarding basic violations in the brightness assumption that will occur at occlusion boundaries, for example. In addition, independently moving objects in the scene will also violate the ego-motion constraint. Preliminary results have shown that the recovered ego-motion estimate is not greatly sensitive to such failures in the models.

In the ego-motion recovery algorithm presented here, the additional change in image brightness introduced by Gaussian or Laplacian blurring within the pyramid have not been modelled. For now, we observe that the recovered ego-motion estimates are often similar at each resolution (see results section), and that error surfaces computed as a function of camera translation using a flow-based, multi-resolution, ego-motion recovery algorithm were similar at all resolutions of analysis [Bergen and Anandan, 1991].

4 Results

The ego-motion algorithm was tested on both natural and computer-rendered image sequences. The motion in the image sequences ranges from approximately 4 to 8 pixels at the original resolution, so we expect that analysis at only the original resolution will not give accurate results since the motion will be outside the range of the incremental motion estimator. In the results presented here, we use four resolutions of analysis. We use $T = (0,0,1)^\top$ and $\Omega = (0,0,0)^\top$ as the initial ego-motion estimate, unless stated otherwise. All local inverse depth estimates are initialised to zero.

Results of the algorithm are shown on computer-rendered images that have size 256×256 pixels, and also on natural images that have size 256×240 pixels. A Laplacian pyramid was used to produce reduced-resolution images of size 128×128, 64×64 and 32×32 pixels for the computer-rendered images, and size 128×120, 64×60 and 32×30 pixels for the natural images. We fit the local surface models to 5×5 pixel windows centered on each point in the image, and the ego-motion model is fitted to each point in the image.

159

We observed that the algorithm can converge to an incorrect solution or fails to converge when analysis begins at a very coarse resolution (corresponding to 16×16 pixels for the image sizes presented here). This behaviour may result from excessive blurring of the image intensities at very coarse scales, and also from the limited number of sample points at very coarse resolutions.

4.1 Computer-rendered images

Figure 1a shows an image pair which have been synthesized and resampled from a known depth map and known ego-motion parameters. For this image pair, we recovered an initial ego-motion estimate by sampling $17 \times 17 = 289$ translation values (see section 2.3) at the coarsest resolution.

Figure 1b shows the difference image between the original image pair. Figure 1c shows the absolute value of the percentage difference between the recovered depth map and the actual depth map. Figure 1d shows the an image of the local surface parameters (inverse depths) such that bright points are nearer the camera than dark points. The bottom portion of the image shows a surface sloping away from the 'camera' towards a ridge at which point the depth changes rapidly. The very top of the image shows the parameters recovered at a blank portion of the image where there is no texture.

Figure 1c aims to show the percentage depth error measure:
$100 * (real\_depth - computed\_depth)/(real\_depth)$. It demonstrates that the errors in the recovered depth map in the foreground portion of the scene are fairly uniform, and actual measurement in a 180×100 window in the foreground gives an rms error of approximately 1%. In the background portion of the scene (just over the ridge) the error is much larger, and measurement in a 100×15 window gives an rms error of approximately 8%. We explain this difference by observing that in both regions the difference between the actual motion and the recovered motion is approximately $0.05 - 0.1$ pixels, whereas the actual motion is approximately $4 - 8$ pixels in the foreground, and approximately 1 pixel in the background. We expect such accuracy in the recovered motion in the foreground and background portions of the image since the image is heavily textured there, but there are large errors in the recovered depth and motion at the very top of the image where there is no texture at all.

Figure 1e shows the recovered ego-motion at each resolution of analysis and also the actual ego-motion. The estimate of ego-motion component at the final

resolution of analysis is very close to the actual ego-motion of the 'camera' despite an occlusion boundary across the center of the image where the brightness constancy assumption is violated. In general, we would expect the least squares minimisation technique to be sensitive to measurement outliers that might be introduced by such deviations in the model. Similar robustness to measurement outliers has also been observed in other motion-fitting techniques that use the same incremental motion estimator (equation 1) within the same coarse-fine analysis framework [Bergen et al. ,1990, Burt et al, 1991]. Burt has recently investigated this noise-rejection phenomenon of the incremental motion estimator in some detail [Burt et al, 1991].

4.2 Natural images

Figure 2a shows the second image of a natural image pair where the image center has been estimated, and where the precise ego-motion is unknown. The image motion in the foreground is approximately 5 pixels towards the camera. Figure 2b shows the inverse depth image recovered at the finest resolution of analysis. The recovered depths are plausible almost everywhere except at the image border and near the recovered focus of expansion (near the gate at the image center). The bright dot at the bottom right hand side of the inverse depth map corresponds to a leaf in the original image that is blowing across the ground towards the camera. We might expect such plausible results from a scene that is heavily textured almost everywhere. Figure 2c shows the computed ego-motion at each resolution of analysis. The initial ego-motion estimate is close to the estimates recovered at the two finest scales, yet the recovered estimates are different at the two coarsest resolutions. At these coarse resolutions, the minimisation procedure followed a low-gradient, incorrect direction in the error surface that led to the incorrect estimates. While this shows how the estimation procedure can recover from following the incorrect minimisation path, it also shows how the error surfaces can differ very slightly between resolutions due to differences introduced by image blurring. In the current implementation of the algorithm, we can choose to prevent minimisation along such low-gradient directions.

Figure 3a shows the second image of a road sequence where there is less image texture. The image motion in the foreground is approximately 9 pixels towards the camera. Figure 3b shows the inverse depth image recovered at the finest resolution of analysis. In this case the inverse depth parameters corresponding

to the top portion of the image (sky) are clearly incorrect, and in fact the local surface parameters should probably not be refined in image regions containing such small image gradients, but for the same reason, such regions have minimal effect on the recovered ego-motion estimate. Figure 3c shows that in this case, the recovered solutions remain close to the initial ego-motion estimate at each resolution. We computed the focus of expansion to lie at the end of the visible portion of the road, at the road center.

4.3 Conclusion

In this paper, we presented an iterative, multi-resolution algorithm that estimates ego-motion directly from image gradients in two images, and we showed how constraints from different local image structures interact with the ego-motion constraint. The ego-motion and depths were recovered quite accurately in the computer rendered example, and the recovered ego-motion and depths appeared plausible in the natural image sequences where ground truth was unavailable. A next step is to investigate how direct, multi-resolution analysis can take advantage of information over multiple frames (> 2) in a sequence.
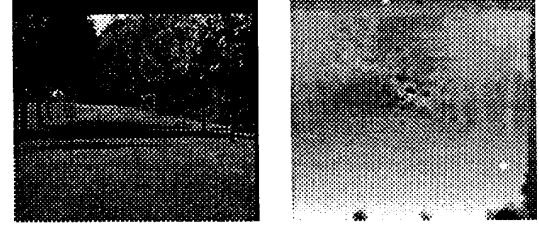
Acknowledgements

References

[Adiv, 1985] Adiv, G. (1985). Determining three-dimensional motion and structure from optical flow generated by several moving objects. *IEEE Trans. on Pattern Analysis and Machine Intelligence*, 7(4):384–401.

[Bergen and Anandan, 1991] Bergen, J. and Anandan, P. (1991) Motion Analysis for Moving Object Detection *In preparation*

[Burt, 1983] Burt, P. and Adelson, E. (1983). The Laplacian Pyramid as a Compact Image Code *IEEE Transactions on Communications*, Com-31(4):532–540

[Burt et al. ,1990] Burt, P., Bergen, J., Hingorani, R., Peleg, S., Anandan, P. (1990) *Proc. of the IEEE Workshop on Intelligent Motion Control*, pages IP75–IP82, Istanbul, Turkey.

[Bergen et al. ,1990] Bergen, J., Burt, P., Hanna, K., Hingorani, R., Jeanne, P. and Peleg, S. (1990). Dynamic Multiple-Motion Computation *Proc. 7th Israeli Conf. on Artificial Intelligence and Image Processing*, pages 149–158, Tel Aviv, Israel.

[Burt et al, 1991] Burt, P., Hingorani, R and Kolczynski, R. (1991). Mechanisms for isolating component patterns in the sequential analysis of multiple motions. *Proc. Workshop on Visual Motion*, Princeton, USA.

[Heeger and Jepson, 1990] Heeger, D. and Jepson, A. (1990). Simple method for computing 3d motion and depth. In *International Conference on Computer Vision*, pages 96–100, Osaka, Japan.

[Heel, 1990] Heel, J. (1990). Direct Estimation of Structure and Motion from Multiple Frames. MIT A.I. Lab Memo No. 1190

[Horn, 1986] B.K.P. Horn, (1986). *Robot Vision*. McGraw-Hill, New York.

[Kearney et al., 1987] Kearney, Thompson, W. and Boley (1987). Optical flow estimation: An error analysis of Gradient-based methods with local optimization. *IEEE Trans. on Pattern Analysis and Machine Intelligence*, 9(2):

[Nagel, 1987] Nagel, H-H. (1987). On the estimation of Optical Flow: Relations between Different Approaches and Some New Results *Artificial Intelligence*, 4:299–323.

[Negahdaripour and Horn, 1987] Negahdaripour, S. and Horn, B. (1987). Direct passive navigation. *IEEE Trans. on Pattern Analysis and Machine Intelligence*, 9(1):168–176.

[Thompson and Pong, 1990] Thompson, W and Pong (1990). Detecting Moving Objects *IEEE Trans. on Pattern Analysis and Machine Intelligence*, 4(1).

Resolution	Ω	T
.	(.0000,.0000,.0000)	(.0000,.0000,1.0000)
32 × 30	(.0027,.0039,-.0001)	(-.3379,-.1352,.9314)
64 × 60	(.0038,.0041,.0019)	(-.3319,-.0561,.9416)
128 × 120	(.0037,.0012,.0008)	(-.0660,-.0383,.9971)
256 × 240	(.0029,.0006,.0013)	(-.0255,-.0899,.9956)

Figure 2: Ego-motion computation on a natural image pair.

a) (top left image) One image of the pair.
b) (top right image) Inverse depth map.
c) (table) Ego-motion estimates at different resolutions.

Resolution	Ω	T
.	(.0004,.0088,.0204)	(.1250,-.7500,.6495)
32 × 32	(.0052,.0053,.0044)	(-.1840,-.4993,.8467)
64 × 64	(.0064,-.0012,.0059)	(.0431,-.4702,.8815)
128 × 128	(.0050,.0001,.0046)	(-.0093,-.5543,.8323)
256 × 256	(.0049,-.0001,.0049)	(.0047,-.5580,.8298)
Actual	(.0050,.0000,.0050)	(.0000,-.5547,.8321)

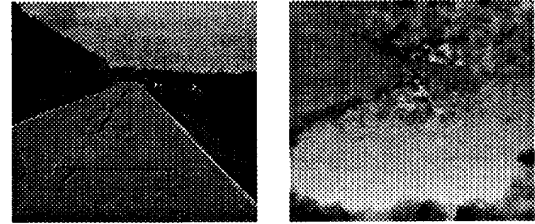Figure 1: Ego-motion computation on a computer-rendered image pair.

a) (top left image) One image of the pair.
b) (top right image) Difference image of the pair.
c) (bottom right image) The percentage depth error measure:
$100 * (real\_depth - computed\_depth)/(real\_depth)$.
d) (bottom left image) Inverse depth map.
e) (table) Ego-motion estimates at different resolutions.

Resolution	Ω	T
.	(.0000,.0000,.0000)	(.0000,.0000,1.000)
32 × 30	(.0024,.0067,.0030)	(-.0297,-.1034,.9942)
64 × 60	(.0022,.0062,.0004)	(-.0103,-.1485,.9887)
128 × 120	(.0022,.0057,.0006)	(.0042,-.1473,.9891)
256 × 240	(.0020,.0056,.0010)	(.0096,-.1560,.9877)

Figure 3: Ego-motion computation on a natural image pair.

a) (top left image) One image of the pair.
b) (top right image) Inverse depth map.
c) (table) Ego-motion estimates at different resolutions.

162